Interfacial Engineering of Vertically-stacked Graphene/h-BN Heterostructure as an Efficient Electrocatalyst for Hydrogen Peroxide Synthesis

Yuying Zhao[1], Xiang Xu[2], Qinxin Yuan[2], Yuhan Wu[2], Kang Sun[3], Bei Li[1], Zeming Wang[4], Ao Wang[1], Hao Sun[1], Mengmeng Fan[2], and Jianchun Jiang[1]

[1]Chinese Academy of Forestry
[2]Nanjing Forestry University
[3]Chinese academy of forestry
[4]Shanghai University

March 22, 2023

Abstract

Recently, in-plane graphene/h-BN (G/h-BN) heterostructure was reported to be the catalytic activity for H_2O_2 synthesis by 2 e^- oxygen reduction reaction (ORR). However, there is rare report for the vertically-stacked G/h-BN heterostructure, which refers to the stacking of graphene domains on the surface of h-BN. Herein, a simulated chemical vapor deposition method was proposed for fabricating abundant vertically-stacked G/h-BN heterostructure by in-situ growing graphene quantum dots (GQDs) on porous h-BN sheets. The catalytic performance of our vertically-stacked heterostructure catalyst is superior to the reported carbon-based electrocatalysts in an alkaline environment, with the H_2O_2 selectivity of 90%-99% in a wide potential range (0.35 V-0.7 V vs. RHE), over 90% faradaic efficiency and high mass activity of 1167 $mmolgcatalyst^{-1}$ h^{-1}. The experimental results and density functional theory simulation verifies that the vertically-stacked heterostructure possesses greatly catalytic performance for 2 e^- ORR and the edge B atoms in the B-centered AB stacking model are the most active catalytic sites. This research well demonstrates the promising catalytic activity for the vertically-stacked G/h-BN heterostructure and provide a facile route for fabricating other vertically-stacked heterostructures.

Interfacial Engineering of Vertically-stacked Graphene/h-BN Heterostructure as an Efficient Electrocatalyst for Hydrogen Peroxide Synthesis

Yuying Zhao#, Xiang Xu#, Qixin Yuan, Yuhan Wu, Kang Sun, Bei Li, Zeming Wang, Ao Wang, Hao Sun, Mengmeng Fan*, Jianchun, Jiang

Y. Zhao, X. Xu, Q. Yuan, Y. Wu, M. Fan

Jiangsu Co-Innovation Center of Efficient Processing and Utilization of Forest Resources, International Innovation Center for Forest Chemicals and Materials, College of Chemical Engineering, Nanjing Forestry University, Nanjing, 210037, China

E-mail: fanmengmeng370@njfu.edu.cn

Y. Zhao, K. Sun, B. Li, A. Wang, H. Sun, M. Fan, J. Jiang Key Lab of Biomass Energy and Material, Jiangsu Province; Jiangsu Co-Innovation Center of Efficient Processing and Utilization of Forest Resources, Institute of Chemical Industry of Forest Products, Chinese Academy of Forestry, Nanjing, 210042, China

Z. Wang

Institute of Nanochemistry and Nanobiology, School of Environmental and Chemical Engineering, Shanghai University, Shanghai, 200444, China

# These two authors contributed equally to this work.

Keywords: graphene/h-BN, vertically-stacked heterostructure, 2 e- pathway, oxygen reduction reaction, hydrogen peroxide synthesis

Abstract: Recently, in-plane graphene/h-BN (G/h-BN) heterostructure was reported to be the catalytic activity for H_2O_2 synthesis by 2 e^-oxygen reduction reaction (ORR). However, there is rare report for the vertically-stacked G/h-BN heterostructure, which refers to the stacking of graphene domains on the surface of h-BN. Herein, a simulated chemical vapor deposition method was proposed for fabricating abundant vertically-stacked G/h-BN heterostructure by *in-situ* growing graphene quantum dots (GQDs) on porous h-BN sheets. The catalytic performance of our vertically-stacked heterostructure catalyst is superior to the reported carbon-based electrocatalysts in an alkaline environment, with the H_2O_2 selectivity of 90%-99% in a wide potential range (0.35 V-0.7 V vs. RHE), over 90% faradaic efficiency and high mass activity of 1167 $mmol_{g_{catalyst}}^{-1}$ h^{-1}. The experimental results and density functional theory simulation verifies that the vertically-stacked heterostructure possesses greatly catalytic performance for 2 e^- ORR and the edge B atoms in the B-centered AB stacking model are the most active catalytic sites. This research well demonstrates the promising catalytic activity for the vertically-stacked G/h-BN heterostructure and provide a facile route for fabricating other vertically-stacked heterostructures.

1. Introduction

With the deep and wide study of two-dimensional materials[1], their heterostructures have shown the exciting prospects for the various next-generation application including electronic, photonic devices[2]. Especially, as the two typically metal-free two-dimensional materials (graphene and h-BN) with greatly similar structure while distinctly different electrochemical properties, the fabricated in-plane and vertically-stacked heterostructures of graphene/h-BN (G/h-BN) produce emergent properties such as quantum Hall effect and phonon polaritons[3].

Graphene or h-BN has been widely used as metal-free electrocatalyst or thermalcatalyst due to their greatly electrochemical or thermochemical properties, respectively. For example, the heteroatoms (N, S, P, et c.) doped graphene was used for electrocatalyzing 4e$^-$oxygen reduction reaction (ORR)[4] and the defect h-BN nanosheets act as the thermalcatalyst for the dehydrogenation of propane to propylene[5]. Since electronic structure of active sites can be well modulated by interfacial engineering to catalyze specific reaction[6]. We speculated that the appropriate graphene/h-BN heterostructure is properly a good candidate as electrocatalyst for some electrochemical reaction. Currently, many researches experimentally and theoretically demonstrated the prospects of in-plane G/h-BN heterostructure in the 2e$^-$ ORR. For instance, the in-plane heterostructure fabricated by embedding h-BN island into carbon matrix shows the O_2 conversion to $H_2O_2$with ˜90% selectivity in an alkaline environment[7]. However, there is no report researching the fabrication and electrocatalytic application of vertically stacked G/h-BN heterostructure. The vertically stacked G/h-BN heterostructure were constructed mainly by mechanical cleavage methods or layer-by-layer transfer techniques, which are obviously not suitable for industrial-scale application[8]. Meanwhile, the low yield and few vertically-stacked heterostructures also limit the further exploration of vertically-stacked heterostructure in the field of catalysis. Therefore, it is imperative to develop a new route for facilely fabricating abundant vertically-stacked heterostructure and meanwhile, the catalytic origin of vertically-stacked heterostructure also needs to be explored.

Among the various topological nanostructures in nano materials, quantum dots, nanometer-sized zero-dimensional structure featured with an enriched density of edge sites are considered to be ideal substrate for fabricating edge active sites[9]. For example, N doped graphene quantum dots have greatly enhanced catalytic performance to 4 e^- ORR by edge doped heteroatom sites[9b]. Given the requirement of abundant active sites in the catalytic application, the abundant edge structure of quantum dots, as fundamental building blocks in vertically-stacked heterostructure will results into abundant heterostructures used as catalytic

sites. Therefore, it's a promising graphene domain for graphene quantum dots (GQDs) deposited on h-BN sheets to fabricate abundant vertically-stacked heterostructures.

Herein, we proposed one-step method for depositing GQDs on porous h-BN (C-BN) to construct abundant vertically-stacked graphene/h-BN heterostructures for electrochemically synthesize H_2O_2 by 2 e^- ORR in an alkaline environment. The morphology characterization shows the uniform distribution of abundant GQDs on h-BN sheets. The vertically-stacked heterostructures abundant catalyst exhibits the excellent catalytic performances including 90%-99% H_2O_2selectivity in a wide potential range (0.35 V-0.7 V vs. RHE) measured by rotating ring-disk electrode (RRDE), over 90% faradaic efficiency during continuous 8 h testing and high mass activity (1167 $mmolg_{catalyst}^{-1}$ h^{-1}) in flow cell testing, superior to the reported metal-free electrocatalysts. The density function theory (DFT) simulation demonstrates the high catalytic performance is derived from the edge B atoms of h-BN interacted with GQDs by van der Waals in the B-centered AB stacking heterostructure model.

Results and discussion

2.1 Morphological Characterization

In Figure 1, B (boric acid), N (dicyandiamide) precursors and the GQDs precursor (1, 3, 6-trinitropyrene) were uniformly mixed by dissolving in DI water and then drying progress. The dried precursor mixture was annealed at 800 for 3 h under NH_3 (200 sccm). In the photograph (Figure S1), the as-prepared GQDs doped porous h-BN (C-BN) shows light brown while the porous h-BN (BN, prepared by no adding GQDs precursor) and the N-doped carbon (N-C, prepared by only 1, 3, 6- trinitropyrene) shows typically white and black, respectively. In order to expose more vertically-stacked G/h-BN heterostructures, the C-BN was further exfoliated into thin nanosheets by liquid N_2pre-processing and then vigorously sonication in isopropanol/DI solution (see method)[10]. In the High-Resolution Transmission Electron Microscopy (HR-TEM) image, abundant GQDs are uniformly dispersed on porous h-BN sheets in the C-BN (Figure 2a) and the diameter distribution of GQDs is located at 5-10 nm. In the selected area Fast Fourier Transfer (FFT) patterns and lattice fringes (Figure 2b, c), the C-BN shows clear spot lattice of (002) and (100) plane corresponding to the (002) plane of h-BN with a 0.33 nm lattice space and the (100) plane of graphene with a 0.20 nm lattice space, respectively[11]. To the contrary, the BN (Figure 2d) just shows obvious (002) spot in the FFT pattern with a 0.33 nm lattice space[11b]. In Figure 2e, the uniform B, N, C element mapping images demonstrate the uniform GQDs distribution on the C-BN nanosheet. Different from GQDs in the C-BN, the N-C just shows amorphous structure with low crystallinity (Figure S2). The various growth processes of carbon structure in C-BN and N-C can be attributed to the substrate of crystal h-BN. In the C-BN, the crystal h-BN domains act as the catalytic substrate for epitaxial growth of crystal graphene structure, which has been widely demonstrated in the vertically-stacked G/h-BN heterostructure preparation by chemical vapor deposition (CVD) method[12]. Compared to the BN (25 °), the degree of (002) peak in C-BN is shifted into higher degree (25.6 °) due to the existence of highly crystal GQDs in the X-ray diffraction (XRD) spectra (Figure 2g). With the increasing of 1, 3, 6-trinitropyrene, the C-BN-x (x representing the doping amount of 1, 3, 6-trinitropyrene, x=20, 50, 100, 200) samples show the gradual increasing degree of (002) peak (Figure 2g inset and Figure S3). The broad and low intensity peaks indicate the amorphous structure in the N-C. In the Raman spectra, the BN and N-C exhibit their typical peaks, the 1377 cm^{-1}peak for h-BN materials[11b, 13] and the D, G peaks for carbon materials[11a], respectively. Compared to the BN, the C-BN has the dispersed typical peak of h-BN materials (Figure S4) indicating the coverage of GQDs on the crystal h-BN domains in the C-BN, which also verifies that the growth mechanism of GQDs on the crystal h-BN domains by a similar CVD progress[12]. The C-BN has a lower SSA (391.8 m^2 g^{-1}) than that of BN (589.2 m^2 g^{-1}) which can be attributed to the "cross-linking agent" (GQDs)[9b] inducing the formation of large sheets. Meanwhile, the addition of GQDs into the C-BN results into the increasing mesopore diameter from 2.1 nm of the BN to 2.3 nm (Figure S5). The N-C has the specific surface area (SSA) up to 2267.8 m^2 g^{-1} with abundant micropores.

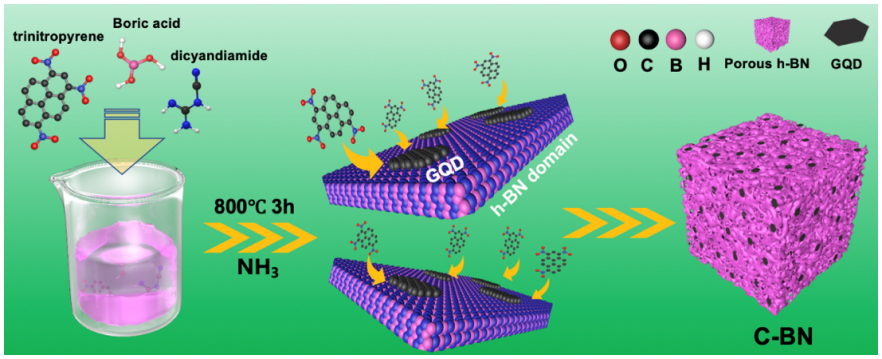

Figure 1 . The preparing progress for C-BN

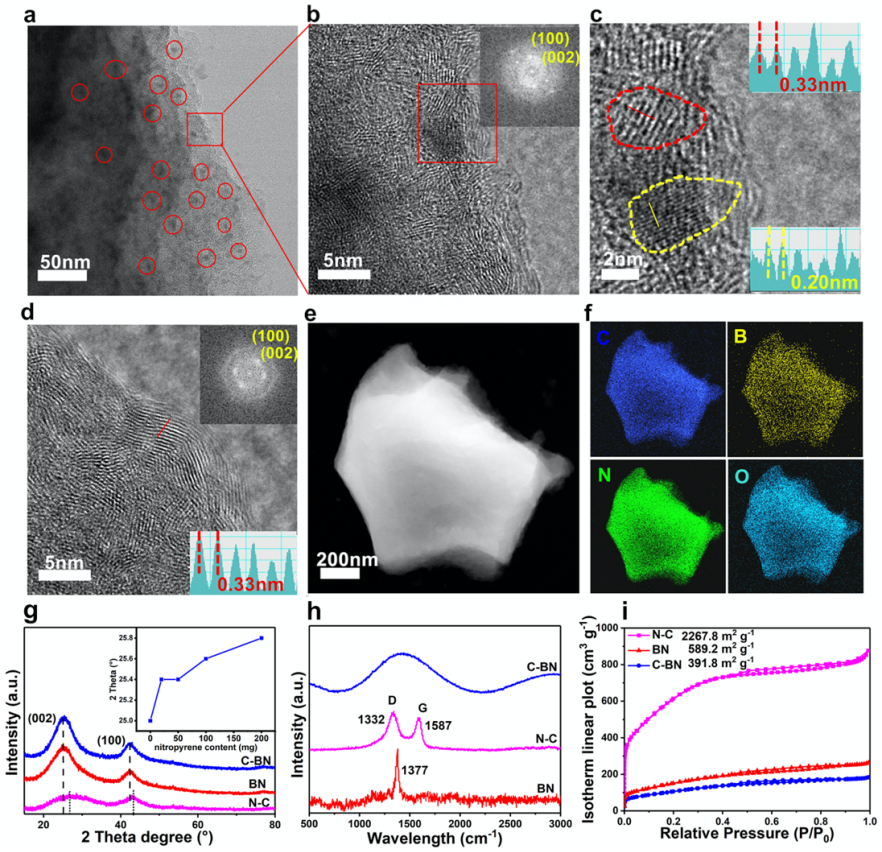

Figure 2 . (a) The synthetic procedure of the C-BN. (b, c) The HR-TEM images of C-BN (the GQDs are remarked with red circles, inset: the FFT patterns of a selected area). (d) The enlarged HR-TEM images of C-BN containing distinct h-BN (red dotted line area) and GQDs (yellow dotted line area) (inset: the corresponding lattice fringes). (e) The HR-TEM image of porous h-BN (inset: the FFT patterns and lattice fringes). (f, g) The HAADF-STEM image of C-BN and the corresponding element mapping images of C (blue), B (yellow), (green), and O (deep blue). (h-j) The XRD patterns, Raman spectra and N_2adsorption-desorption isotherms of porous h-BN, C-BN and N-C.

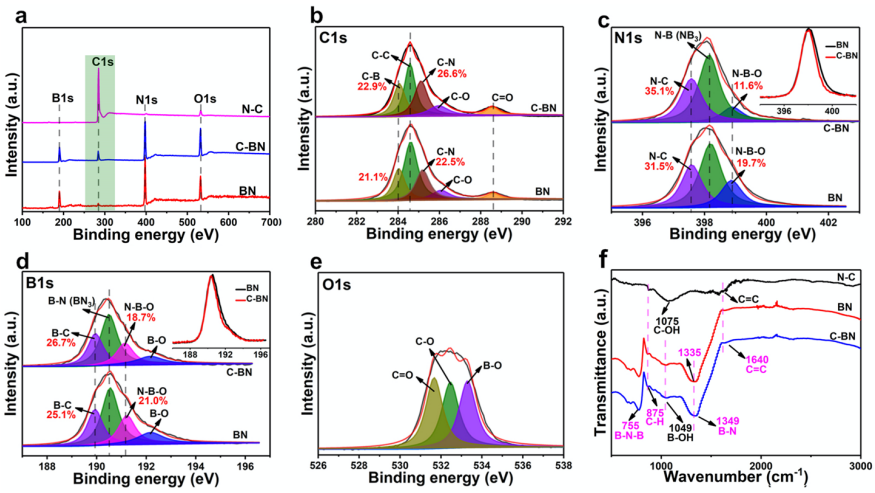

Figure 3 . (a) The XPS survey spectra of all samples. (b-d) The high-resolution C1s, N1s, B1s spectra of C-BN, and porous h-BN. e) The high-resolution O1s of C-BN. (f) The FT-IR spectra of C-BN, porous h-BN and N-C.

The chemical composition and heteroatoms configuration were investigated by X-ray photoelectron spectroscopy (XPS). Compared to the BN, the high C content appears in the C-BN due to the existence of GQDs in Figure 3a, and with the increasing amount of 1, 3, 6-trinitropyrene, the C contents gradually increase for the C-BN-x samples (Tables S1). In the C1s spectra of BN (Figure 3b), the appearance of C-B (22.5% accounting to all C species, unless stated otherwise, all relative content is accounting for all species) and C-N (21.1%) peaks can be attributed to the C impurity as demonstrated in our previous study[11b]. Compared to the BN, the C-BN shows slightly higher C-N (26.6%) and C-B (22.9%) contents indicating the enhanced interaction between BN nanosheets and GQDs (Figure 3b), which can be attributed to some in-plane hybridizations of GQDs and h-BN domains[11b, 14]. In the N1s spectra (Figure 3c), the N1s peak of C-BN is shifted into higher binding energy than that of the BN demonstrating the formation of many N-C bonds, and the shift into lower binding energy of C-BN in the B1s spectra (Figure 3d) suggests the formation of many B-C bonds[11b]. In the N1s and B1s spectra, the BN and C-BN all show main B-N (NB_3 or BN_3) peak demonstrating the formation of h-BN domains. The N-B-O content of C-BN in the N1s and B1s spectra decreases from 19.7% of the BN to 11.6% and from 21% to 18.7%, respectively, which can be attributed to the formation of many C-B and C-N bonds by the edge N-B-O groups of h-BN domains and the edge C atoms of GQDs due to some in-plane hybridizations[11b, 14]. In the O1s spectra (Figure 3e), the C-BN also contains many oxygen species including C=O, C-O and B-O. In the Fourier Transform Infrared Spectroscopy (FT-IR) spectra, two strong peaks are observed at 1349 and 755 cm^{-1} corresponding to the B-N and the B-N-B in the BN and C-BN, demonstrating the existence of h-BN domains[15]. Compared to the BN, the C-BN has obviously enhanced C=C peak at 1640 cm^{-1} indicating the existence of GQDs (Figure 3f)[16]. The B-N-B peak of C-BN shows weaker intensity than that of BN which can be attributed to the cover of GQDs on the surface of h-BN domains (Figure S6)[17].

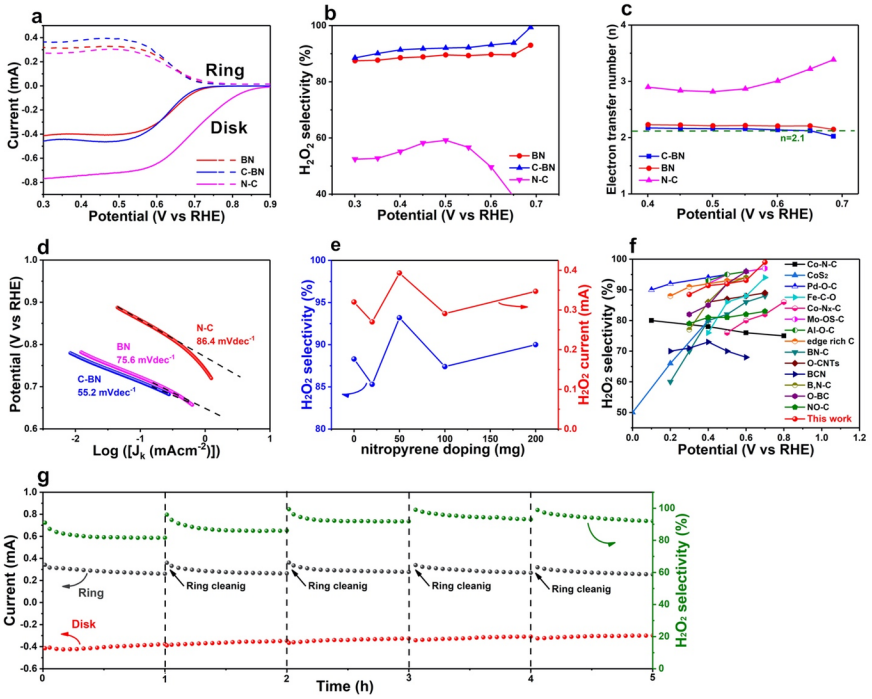

Figure 4 . (a) The LSV curves of C-BN, porous h-BN and N-C (solid lines) together with the corresponding H_2O_2 current on the ring electrode (dashed lines) at a fixed potential of 1.2 V vs. RHE in O_2-saturated 0.1 M KOH solution at 1600 rpm. (b, c) The calculated H_2O_2 selectivity and electron transfer number according to the LSV curves. (d) The Tafel curves of all samples. (e) The comparison of H_2O_2selectivity and ring current at 0.5 V vs. RHE for C-BN-x samples. (f) The comparison of H_2O_2 selectivity to many recently reported electrocatalysts in the alkaline solution measured by the similar RRDE method. (g) The stability test of C-BN at a fixed disk potential of 0.5 V vs. RHE with the speed of 1600 rpm in O_2 saturated electrolyte and the Pt ring was recovered once an hour.

2.2 Electrocatalytic Performance toward H_2O_2 Generation

In order to measure the 2 e^- ORR performance, a standard three-electrode Rotating Ring Disc Electrode (RRDE) was applied with the O_2-saturaed electrolyte of 0.1 M KOH. The electrolyte was out of light during electrochemical testing to reduce the H_2O_2 decomposition and the results show that low-concentration H_2O_2 has a negligible degradation rate (Figure S7). The ring electrode was held at 1.2 V vs. RHE to oxidize the produced H_2O_2 formed at disk electrode in the RRDE measurement[18]. The H_2O_2 collection efficiency was calibrated to be 0.37 by redox reaction of $[Fe(CN_6)]^{4-}/[Fe(CN_6)]^{3-}$in Figure S8. After the liquid N_2 assisted exfoliation process, the separated thin nanosheets dispersed into highly-conductivity carbon black (2 mg ml^{-1}) were used as the catalyst ink. As shown in Figure 4a, all catalysts exhibit ORR polarization curves with the disk current (solid line) produced from O_2 reduction and the ring current (dashed line) from H_2O_2 oxidation. Compared to the bare glassy carbon electrode (GCE), the C-BN loading on GCE shows much higher ring current and more positive onset potential (Figure S9), which demonstrates the much abundant catalytic sites with high activity in the C-BN. The C-BN and BN have similar disk current curves but the former shows higher ring current indicating the higher catalytic activity to 2 e^- ORR. Although the N-C shows higher disk current and onset potential, the low ring current reveals the low 2 e^- ORR catalytic activity due to many N species[19] (Figure S10) and abundant edge structure[20]. The H_2O_2 selectivity was calculated based on the LSV curves according to the equations (supporting information). The C-BN shows the highest H_2O_2 selectivity of 90%-99% in the wide range of 0.35 V-0.70 V vs. RHE and the electron transfer number is 2.1 close to the ideal two electron pathway (Figure 4b, c). Compared to BN (75.6 mV dec^{-1}) and N-C

(86.4 mV dec^{-1}), the C-BN has the lowest Tafel value of 55.2 mV dec^{-1} demonstrating the higher catalytic activity in the C-BN (Figure 4d). In order to optimized GQDs structure in the C-BN, various amount of C precursor (1, 3, 6-trinitropyrene) was added and the corresponding samples are named as C-BN-x (x =20 mg, 50 mg, 100 mg, 200 mg). The catalytic measurement demonstrates that the performance of C-BN-x samples exhibit a volcano trend in terms of H_2O_2 selectivity and ring current (Figure 3e, Figure S11) and the C-BN-50 shows the highest H_2O_2 selectivity (93.2%) and ring current (0.39 mA) at 0.5 V vs. RHE. The lower catalytic performance for C-BN-100, -200 can be attributed to the carbon accumulation into large scale sheets leading to few vertically-stacked heterostructures as shown in the HR-TEM image (Figure S12). The H_2O_2 selectivity of the optimized C-BN was further compared with many recently reported metal-based and carbon-based electrocatalysts (Figure 4f and Table S2), and the H_2O_2 selectivity of C-BN is superior to most of reported electrocatalysts. The catalytic stability was further tested by current-time curve with the RRDE measurement. A gradual degradation of ring current during stability test was mainly due to the surface oxidation of Pt ring electrode constantly operated at high potential (1.2 V vs. RHE), so the Pt ring electrode was readily recovered by rapid cyclic voltammetry at low potentials once an hour to reduce PtO_x (Figure 4g)[21]. The C-BN shows a stable H_2O_2 selectivity of above 90% over the 5 h continuous operation demonstrating the high electrochemical stability.

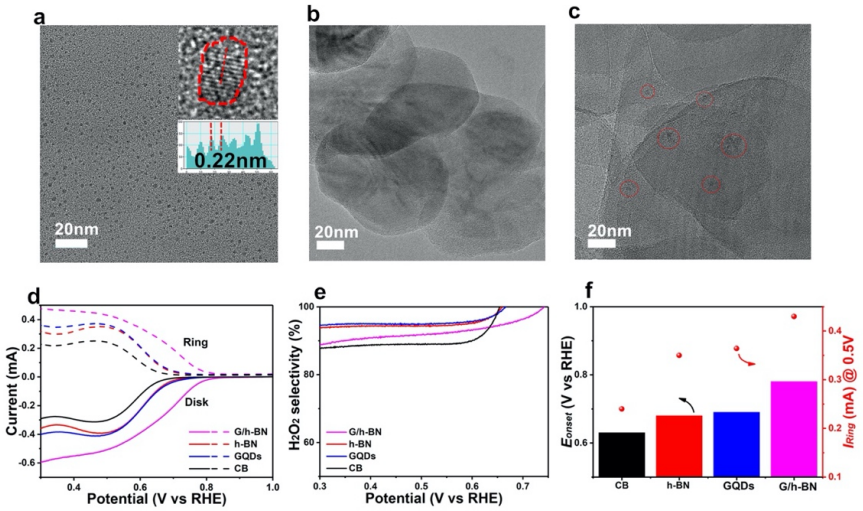

Figure 5 . (a) The HR-TEM image of GQDs (inset: the corresponding lattice fringes). (b) The HR-TEM image of exfoliated commercial h-BN nanosheets. (c) The HR-TEM image of G/h-BN and the GQDs are remarked with red circles. (d) The LSV curves of carbon black, h-BN, GQDs and G/h-BN (solid lines) together with the corresponding H_2O_2 currents on the ring electrode (dashed lines). (e) The calculated H_2O_2selectivity according to the LSV curves. (f) The comparison ofE_{onset} at I_R= 0.05 mA and ring current for different samples.

In order to demonstrate the catalytic activity of vertically-stacked G/h-BN heterostructures, we fabricated a similar vertically-stacked heterostructures catalyst by mixing pre-prepared GQDs and commercial h-BN nanosheets. As shown in Figure 5a, the GQDs prepared by hydrothermal reaction of 1, 3, 6-trinitropyrene show uniform size distribution with the diameter of 3-5 nm and a 0.22 nm lattice space (Figure 4a inset). The h-BN nanosheets have good crystallinity (Figure S13) and their size is mainly located at 200-300nm (Figure 5b). After overnight magnetic stirring, the GQDs are dispersed on h-BN sheets (Figure 5c). The RRDE was applied to measure the catalytic performance and the measuring conditions are same to those of C-BN. Compared to the GQDs and h-BN, the G/h-BN shows the higher disk, ring current and more positive onset potential (Figure 5d) indicating the high catalytic activity. The H_2O_2 selectivity is calculated to be 90%-97% in 0.35-0.7 V vs. RHE (Figure 5e). The high selectivity of GQDs (˜95%) and h-BN (˜94%) in 0.3-0.6 V vs.

RHE can be derived from the abundant edge structure because there are many reports have demonstrated that the graphene edge and h-BN nanosheet edge are the effective active sites for catalysis[5, 22]. Therefore, the G/h-BN shows a higher catalytic performance in terms of onset potential and ring current (Figure 5f), which can well confirm our previous conclusion that many specific atoms at the vertically-stacked G/h-BN heterostructures are the main catalytic sites.

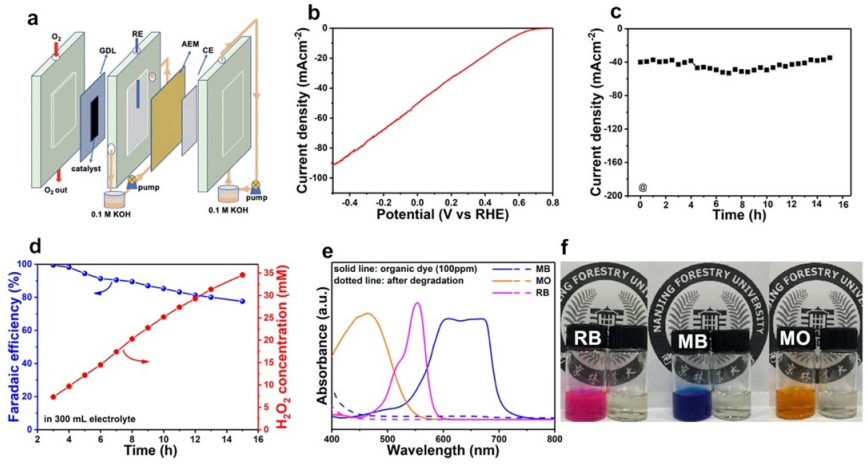

Figure 6 . (a) The schematic illustration of flow cell setup. (b) The LSV curve of flow cell setup with the C-BN/carbon black as the catalyst in cathode. (c) The i-t curve at 0.2 V vs. RHE for the H_2O_2 production in the flow cell. (d) The FE and H_2O_2 concentration in the flow cell during 15 h testing. (e) The Uv-vis spectra of RB, MB and MO solution before and after adding electrolyte. (f) The photograph of dye solution (50 ppm) before and after treatment.

In order to explore the practical application of C-BN catalyst, a flow cell setup was applied in Figure 6a and Figure S14. The C-BN nanosheets mixing with conductive carbon black acts as the catalyst ink. A gas diffusion layer (GDL) with the concentration of 1 mg cm^{-2} as cathode, Pt film as anode, Ag/AgCl as reference electrode and 0.1 M KOH as the electrolyte. The current density rapidly reaches to 90 mA cm^{-2} at -0.5 V vs. RHE in this flow setup in Figure 6b. The stability was measured by i-t curve at a fixed potential of 0.2 V vs. RHE corresponding the current density of ~40 mA cm^{-2}, and the current density is almost no change after continuous 15 h testing in Figure 6c. The H_2O_2 in the electrolyte was detected by the Ce^{4+} titration method[18a] (Figure S15) and the H_2O_2 concentration was gradually increasing to 35 mM in 300 ml electrolyte (produced H_2O_2 amount: 357 mg) by prolonging reaction time to 15 h in Figure 6d. The average reaction rate is up to 1167 $mmolg_{catalyst}^{-1}h^{-1}$ (calculated by the concentration of carbon black) higher than most of catalysts (Table S3). The Faradaic efficiency (FE%) is calculated to be over 90 % at first 8 h and the FE% retains over 80% after 15 h testing. The retained FE% is higher than the reported electrocatalysts measured by a flow cell setup[23]. The decreasing FE% after long-time testing can be attributed to the increasing H_2O_2 decomposition reaction rate with H_2O_2accumulation[23]. The dye degradation experiment was completed with containing H_2O_2electrolyte to explore the potential application of electrochemically synthesized H_2O_2. The pH of electrolyte (5 ml, 35 mM) was modulated to be 2.0 and then the electrolyte was mixed with various dyes (1.5 ml, 200 ppm) including Rhodamine B (RB), methylene blue (MB) and methyl orange (MO). Fe^{2+} was added into above mixing solution to induce the Fenton reaction and the produced hydroxyl radical can effectively degrade dyes[24]. After the degrading reaction, the typical absorption peaks of RB, MB and MO disappear in UV-vis spectra (Figure 6e) and the mixture solution rapidly becomes colorless in 20 s after adding Fe^{2+} (Figure 6f).

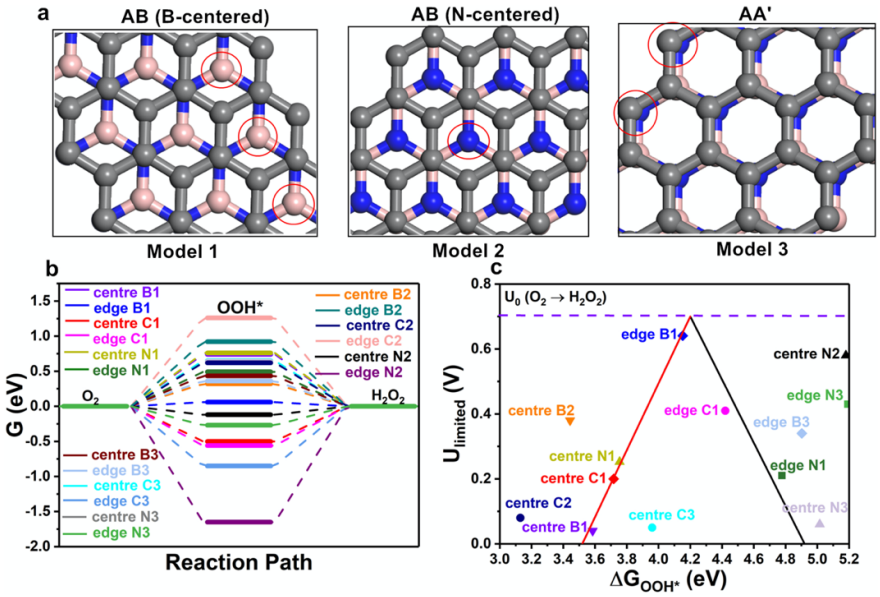

Figure 7 . The vertically-stacked G/h-BN heterostructure models (a): B-centered AB stacking (model 1), N-centered AB stacking (model 2) and AA' stacking (model 3). (b) The illustration of 2 e^- ORR base reaction pathway on the different atoms. The active atoms are remarked by red circles. (c) The volcano plot between ΔG_{OOH^*} and the 2 e^- ORR $U_{limited}$ for the optimized models and the purple dotted line representing equilibrium potential of O_2/H_2O_2. Pink, blue, and gray balls indicate B, N, and C atoms, respectively.

2.3 DFT Simulation

In order to explore the catalytic sites in the vertically-stacked G/h-BN heterostructure, the DFT simulation was applied. Due to the greatly similar lattice structure between h-BN and graphene, we used the in-plane lattice parameter of graphene for both supercell calculations to directly compare the potential active atoms from graphene and h-BN in the vertically-stacked G/h-BN heterostructure[3b]. Three kinds of stacking configurations for the monolayer G/h-BN interface[3b] (B-centered AB stacking, N-centered AB stacking and AA' stacking, corresponding to model 1, 2, 3, respectively) were given as shown in Figure 7a. There are two kinds of C atoms (edge C and planar C) in the graphene and two kinds of B atoms (edge B and planar B) and N atoms (edge N and planar N) in the h-BN.

In the 2 e^- ORR, O_2 is converted to H_2O_2 involving two coupled electrons:

$O_2 + * + H_2O + e^- \; OOH^* + OH^-$ (6)

$OOH^* + H_2O + e^- * + H_2O_2$ (l) $+ OH^-$ (7)

The reaction rate of O_2 to OOH* is greatly dependent on the reaction potential barrier. For an ideal model, the reaction free energies (G) for all electron-transfer steps are zero when the applied potential equals equilibrium potential[25]. Compared to the C, N atoms in different models, the edge B atom in B-centered AB stacking model (edge B1) achieves a highest reaction rate in the same condition because its G is 0.06 eV close to zero (Figure 7 b and Table S4)[26]. Moreover, the planar N in N-centered AB stacking model (center N2, G=-0.12 eV) and edge N atom in AA' stacking model (edge N3, G=-0.27 eV) also show low free energies in the corresponding models. The limiting potential ($U_{limited}$) is a metric of activity as the lowest potential at which all the reaction steps are downhill in free energy[23, 27]. The theoretical overpotential represents the maximum difference between the $U_{limited}$ and equilibrium potential. In Figure 7c and Table S4, various models are located in a volcano plot and the left-side sites show strong adsorption energy of OOH* (ΔG_{OOH^*}) (equation 7 is a limiting step) while the right-side sites have weak adsorption energy (equation 6

is a limiting step)[26]. In our research, the alkaline environment (pH=13, 0.1M KOH) make H_2O_2molecule to deprotonate and form HO_2^-. Although there is little difference for their (H_2O_2/HO_2^-) formation free energies, the volcano plots in the form of H_2O_2 can provide a more general mechanism[25]. Compared to the other models, the edge B1 site shows the energy of 4.15 eV approaching the ideal standard free energy of 4.22 eV (The ΔG_{OOH*} of 4.22 eV corresponding to the thermodynamic equilibrium potential, U_0 = 0.70 V[23]). The $U_{limited}$ of edge B1 site is 0.64 V close to the lowest potential of 0.70 V. The appropriate adsorption energy and low $U_{limited}$ demonstrate the edge B1 has the highest catalytic activity to H_2O_2[25]. Compared to model 2 and 3, the C, N, B atoms in model 1 are located at the volcano curves indicating the more appropriate vertically-stacked G/h-BN heterostructure for 2 e^- ORR.

Conclusion

One "simulated CVD" method was proposed to fabricate vertically-stacked G/h-BN heterostructure by grow GQDs to the h-BN nanosheets. As reported in many papers, the formation of crystal GQDs was dependent to the h-BN substrate. The prepared vertically-stacked G/h-BN heterostructure (C-BN) shows high 2 e^- ORR performance especially, H_2O_2 selectivity in a wide potential range and stability. A simulating vertically-stacked G/h-BN heterostructure also verify the greatly enhanced effect of heterostructure on the 2 e^- ORR performance. The flow cell test further demonstrates the promising practical application of our heterostructure catalyst. According to the DFT simulation, the B-centered AB stacking is the optimal heterostructure for 2 e^- ORR, and its edge B atoms are considered to be the key active sites. Therefore, this paper provides one new kind of catalytic site for various catalytic fields.

Experimental section

*Synthesing C-BN, prous h-BN and N-C :*Boric acid (0.618 g), dicyandiamide (2.7 g), 1, 3, 6 - trinitropyrene (50 mg) were dispersed into 50 ml deionized water in a 200 ml beaker and then above solution was sonicated for 1 h (200 W). The solution was fiercely stirred and heated on a hot plate until all water completely evaporated. The obtained solid was ground into powders in a mortar and then calcined at 800 °C for 3 h under NH_3 (50 sccm) in a resistance-heating horizontal furnace. After cooling to room temperature, we can get porous C-BN samples. In order to control the C content, various 1, 3, 6 – trinitropyrene amounts (20, 100 or 200 mg) were added and the corresponding samples were defined as C-BN-20, -100 and -200, respectively. The porous h-BN was prepared by the same progress except no addition of trinitropyrene. The N-C was prepared by directly annealing trinitropyrene at 800 °C for 3 h under NH_3 (50 sccm). The commercial h-BN powders were purchased from Sigma-Aldrich. The 1, 3, 6 – trinitropyrene was prepared according to the previous research[11a].

Liquid N_2 assisted Exfoliation: The sample (C-BN, BN and commercial h-BN) was placed in liquid N_2 for 20 min and then the solution (isopropanol: DI (V/V) =1:1) was quickly added with the concentration of 1 mg ml^{-1}[10]. The mixing solution was continuously sonicated for 10 h (200 W). The exfoliated nanosheets are separated by centrifugation (3000 rpm, 5min). The supernatant is used for the application of catalyst ink.

Model experiments: The GQDs was prepared according to the previous research[11a]. The 40 μl GQDs in isopropanol (2.5 mg ml^{-1}) and 200 μl supernatant of exfoliated commercial h-BN was mixed and diluted to 1 ml with isopropanol. After overnight magnetic stirring, 5 wt% Nafion solution (50 μl) and carbon black (2 mg) were added into the solution. After the sonication (200 W, 2 h), the G/h-BN catalyst ink was prepared. The other measuring conditions are same to those of C-BN.

Electrochemical characterization : All the electrochemical tests were carried out in an electrochemical workstation (Chenhua CHI760E) with a three-electrode system. A RRDE electrode with a disk glassy carbon electrode area of 0.2475 cm^{-2} and Pt ring area of 0.1866 cm^{-2} was used as the working electrode. A graphite rod and a Hg/HgO electrode acted as the counter electrode and reference electrode, respectively. The supernatant (1 ml) after the liquid N_2-assisted exfoliation was mixed with carbon black (2 mg) and 5wt% Nafion solution (50 μl) by sonication (200 W, 2h) as the catalyst ink. 10 μl ink was dopped onto RRDE electrode and dried at room temperature. Linear sweep voltammetry (LSV) curves were conducted in O_2 saturated 0.1 M KOH solution at a scan rate of 10 mV s^{-1} at the speed of 1600 rpm. The solution resistance (R_s) was

not compensated. A potential of 1.2 V vs. RHE was applied at the ring electrode. The H_2O_2 selectivity and electron transfer number were calculated by the following equations based on the LSV curves.

H_2O_2 yield (%) = $200\times\frac{I_R/N}{I_D+I_R/N}$ (1)

N = $\frac{4|\ I_D|}{I_D+I_{R/N}}$ (2)

Where I_R is the ring current, I_D is the disk current, and N is the collection efficiency (0.37 after calibration).

Electrochemical measurement in a flow cell: A flow cell setup is a two-compartment cell with a cation exchange membrane as a separator. 150 µl C-BN catalyst ink (1 ml supernatant with 4 mg carbon black) was deposited on the gas diffusion layer electrode (GDL, HESEN HCP120) (working area 1 cm^2) with a loading of 0.6 mg cm^{-2} (the amount of carbon black) as the cathode. The Pt film and Ag/AgCl electrode were used as the anode and reference electrodes, respectively. In the two compartments, 0.1 M KOH (300 mL) was used as the electrolyte and was recycled through each compartment at the flow rate of 20 ml min^{-1}. O_2 was fed at the rate of 40 ml min^{-1} to the cathode. The electrosynthesis of H_2O_2 was performed at a fixed potential 0.2 V vs. RHE.

The faradaic efficiency (FE) of H_2O_2 was calculated according to the following equation:

FE (%) = $\boldsymbol{2CVF/Q}$ * 100% (3)

where C represents the concentration of H_2O_2 (mol l^{-1}) in the electrolyte, V the volume of electrolyte (l), F Faraday constant (96485 C mol^{-1}), Q total charge amount (C) during the reaction. The Q was determined by integral operation in the electrochemical workstation:

The H_2O_2 concentration in the electrolyte was measured by a titration method using $Ce(SO_4)_2$. The adding of H_2O_2 leads to the conversion from yellow Ce^{4+} to colorless Ce^{3+} in the following reaction:

$2Ce^{4+} + H_2O_2 = 2Ce^{3+} + 2H^+ + O_2$ (4)

According to the equation, the$C_{\ H2\ O2}$ was calculated based on the equation:

$C_{H2O2} = 1/2\ \Delta C_{\ Ce4+}$ (5)

UV-V is spectroscopy was used to make the linear calibration curve between Ce^{4+} concentration and the Ce^{4+} absorbance at 317 nm.

Characterization: The morphology was characterized by high-resolution TEM (FEI Talos F200s) with Energy dispersive X-ray element detector (FEI Super-X EDS Detector). The structure and composition were characterized by X-ray photoelectron spectra (Thermo Scientific Al K_α), X-ray diffractometer (Bruker, D8 FOCUS) equipped with a Cu K_α radiation source (λ=0.154 nm), FT-IR (Nicolet IS10). The Raman spectra were measured by a Renishaw inVia with a 532 nm laser source. The surface area and meso/macropore size distributions of the as-prepared materials were determined by the Brunauer-Emmett-Teller (BET) and Barret-Joyner-Halenda (BJH) methods, respectively. N_2 adsorption-desorption isotherm tests were performed on a gas adsorption analyzer (ASAP2460, Micromeritics).

DFT simulation: We used the Vienna Ab-initio Simulation Package (VASP, 5.4.4) code54, 55 with GGA-PBE exchange-correlation functional56 for DFT calculations[28]. The project-augmented wave (PAW) pseudopotential57, 58 for describing the core-valence interactions and cutoff of 450 eV were used[29]. h-BN and graphene were known to have very similar lattice constant ($a_{h\text{-}BN}$ = 2.504 [30] and $a_{Graphene}$ = 2.464 [31]). In this study, we performed two monomer calculations using graphene's in-plane lattice parameters to directly compare the screening effects of each material. Furthermore, we assumed a thickness of ˜20 for the vacuum layer to prevent the interaction between periodic images. In addition, we considered three different stacked configurations (AA' stacking, B-centered AB stacking, and N-centered AB stacking) for the monolayer h-BN/Graphene interface. The Brillouin zone in reciprocal space was sampled using Monkhorst-Pack scheme59, and the geometric/electronic structure optimization was performed using 1×1×1 and 2×2×1 k point meshes[32].

The Gibbs free energy of the 2 e^- ORR elementary steps is calculated using the computational hydrogen electrode (CHE) model, defined as ΔGn (U) = ΔGn (U = 0) + neU, where n is the number of e^- transferred in reaction and U is the potential of the electrode to the reversible hydrogen electrode (RHE)[33]. At U=0V, ΔGn = ΔEn – ΔS + ΔZPE, where ΔEn is DFT-calculated reaction energy in vacuum, TΔS is the entropy contributions to reaction at T = 298.15 K, ΔZPE is zero-point energy (ZPE) correction based on the calculated vibrational frequencies. The free energy of O_2(g) was derived as $G_{O2(g)} = 2G_{H2O(l)} - 2G_{H2} - 4 \times 1.23$ eV since the high-spin ground state of an oxygen molecule is notoriously poorly described in DFT calculations.

Acknowledgements

This work was supported by "National Natural Science Foundation of China (No. 51902162)", the Foundation Research Project of Jiangsu Province (BK20221338), Jiangsu Co-Innovation Center of Efficient Processing and Utilization of Forest Resources, International Innovation Center for Forest Chemicals and Materials, Nanjing Forestry University, merit-based funding for Nanjing innovation and technology projects, and the Foundation of Jiangsu Key Lab of Biomass Energy and Material (JSBEM-S-202101).

Author Contributions

Y.Y.Z. and X.X. contributed equally to this work. X.X., Y.Y.Z. and M.M.F. performed the major experiments. Q.X.Y., Y.H.W., K.S., B.L., H.S., and A.W. performed the experiments. M.M.F. and Y.Y.Z. wrote the paper. W.C., J.C.J. supervised the whole study. All authors read and approved the final manuscript.

Reference

[1] C. Chang, W. Chen, Y. Chen, Y. Chen, Y. Chen, F. Ding, C. Fan, H. Jin Fan, Z. Fan, C. Gong, Y. Gong, Q. He, X. Hong, S. Hu, W. Hu, W. Huang, Y. Huang, W. Ji, D. Li, L.-J. Li, Q. Li, L. Lin, C. Ling, M. Liu, N. Liu, Z. Liu, K. Ping Loh, J. Ma, F. Miao, H. Peng, M. Shao, L. Song, S. Su, S. Sun, C. Tan, Z. Tang, D. Wang, H. Wang, J. Wang, X. Wang, X. Wang, A. T. S. Wee, Z. Wei, Y. Wu, Z.-S. Wu, J. Xiong, Q. Xiong, W. Xu, P. Yin, H. Zeng, Z. Zeng, T. Zhai, H. Zhang, H. Zhang, Q. Zhang, T. Zhang, X. Zhang, L.-D. Zhao, M. Zhao, W. Zhao, Y. Zhao, K.-G. Zhou, X. Zhou, Y. Zhou, H. Zhu, H. Zhang, Z. Liu, *Acta Phys. Chim. Sin.***2021** , 0, 2108017.

[2] P. Solís-Fernández, M. Bissett, H. Ago, *Chem. Soc. Rev.***2017** , 46, 4572.

[3] Q. Li, M. Liu, Y. Zhang, Z. Liu, *Small* **2016** , 12, 32.

[4] P. Wang, W. Lee, J. P. Corbett, W. H. Koll, N. M. Vu, D. A. Laleyan, Q. Wen, Y. Wu, A. Pandey, J. Gim, D. Wang, D. Y. Qiu, R. Hovden, M. Kira, J. T. Heron, J. A. Gupta, E. Kioupakis, Z. Mi,*Adv. Mater.* **2022** , 34, e2201387.

[5] M. Fan, Y. Huang, F. Yuan, Q. Hao, J. Yang, D. Sun, *J. Power Sources* **2017** , 366, 143.

[6] M. Fan, Z.-Q. Feng, C. Zhu, X. Chen, C. Chen, J. Yang, D. Sun,*J. Mater. Sci.* **2016** , 51, 10323.

[7] X. Zhang, R. You, Z. Wei, X. Jiang, J. Yang, Y. Pan, P. Wu, Q. Jia, Z. Bao, L. Bai, M. Jin, B. Sumpter, V. Fung, W. Huang, Z. Wu,*Angew. Chem. Int. Ed.* **2020** , 59, 8042.

[8] Y. Zhang, Y. Lin, T. Duan, L. Song, *Mater. Today***2021** , 48, 115.

[9] S. Chen, Z. Chen, S. Siahrostami, D. Higgins, D. Nordlund, D. Sokaras, T. R. Kim, Y. Liu, X. Yan, E. Nilsson, R. Sinclair, J. K. Nørskov, T. F. Jaramillo, Z. Bao, *J. Am. Chem. Soc.***2018** , 140, 7851.

[10] C. R. Dean, A. F. Young, I. Meric, C. Lee, L. Wang, S. Sorgenfrei, K. Watanabe, T. Taniguchi, P. Kim, K. L. Shepard, J. Hone,*Nat. Nanotechnol.* **2010** , 5, 722.

[11] S. J. Haigh, A. Gholinia, R. Jalil, S. Romani, L. Britnell, D. C. Elias, K. S. Novoselov, L. A. Ponomarenko, A. K. Geim, R. Gorbachev,*Nat. Mater.* **2012** , 11, 764.

[12] L. Xiao, X. Liu, R. Zhou, T. Zhang, R. Zhou, B. Ouyang, E. Kan, P. J. Cullen, K. Ostrikov, X. Tu, *Energ. Convers. Manage.***2021** , 231.

[13] M. Fan, C. Zhu, J. Yang, D. Sun, *Electrochim. Acta***2016** , 216, 102.

[14] Y. Wang, Y. Liu, J. Zhang, J. Wu, H. Xu, X. Wen, X. Zhang, C. S. Tiwary, W. Yang, R. Vajtai, Y. Zhang, N. Chopra, I. N. Odeh, Y. Wu, P. M. Ajayan, *Sci. Adv.* 3, e1701500.

[15] L. Wang, Y. Wang, T. Xu, H. Liao, C. Yao, Y. Liu, Z. Li, Z. Chen, D. Pan, L. Sun, M. Wu, *Nat. commun.* **2014** , 5, 5357.

[16] M. Fan, J. Wu, J. Yuan, L. Deng, N. Zhong, L. He, J. Cui, Z. Wang, S. K. Behera, C. Zhang, J. Lai, B. I. Jawdat, R. Vajtai, P. Deb, Y. Huang, J. Qian, J. Yang, J. M. Tour, J. Lou, C.-W. Chu, D. Sun, P. M. Ajayan, *Adv. Mater.* **2019** , 31, 1805778.

[17] T. Gao, X. Song, H. Du, Y. Nie, Y. Chen, Q. Ji, J. Sun, Y. Yang, Y. Zhang, Z. Liu, *Nat. commun.* **2015** , 6, 6835.

[18] S. Tang, H. Wang, H. S. Wang, Q. Sun, X. Zhang, C. Cong, H. Xie, X. Liu, X. Zhou, F. Huang, X. Chen, T. Yu, F. Ding, X. Xie, M. Jiang, *Nat. commun.* **2015** , 6, 6499.

[19] W. Yang, G. Chen, Z. Shi, C.-C. Liu, L. Zhang, G. Xie, M. Cheng, D. Wang, R. Yang, D. Shi, K. Watanabe, T. Taniguchi, Y. Yao, Y. Zhang, G. Zhang, *Nat. Mater.* **2013** , 12, 792.

[20] M. Fan, J. D. Jimenez, S. N. Shirodkar, J. Wu, S. Chen, L. Song, M. M. Royko, J. Zhang, H. Guo, J. Cui, K. Zuo, W. Wang, C. Zhang, F. Yuan, R. Vajtai, J. Qian, J. Yang, B. I. Yakobson, J. M. Tour, J. Lauterbach, D. Sun, P. M. Ajayan, *ACS Catal.* **2019** , 9, 10077.

[21] L. Ci, L. Song, C. Jin, D. Jariwala, D. Wu, Y. Li, A. Srivastava, Z. F. Wang, K. Storr, L. Balicas, F. Liu, P. M. Ajayan,*Nat. Mater.* **2010** , 9, 430.

[22] Z. Luo, Y. Fang, M. Zhou, X. Wang, *Angew. Chem. Int. Ed.***2019** , 58, 6033.

[23] T. Van Tam, S. G. Kang, K. F. Babu, E.-S. Oh, S. G. Lee, W. M. Choi, *J. Mater. Chem. A* **2017** , 5, 10537.

[24] X. Yu, P. Han, Z. Wei, L. Huang, Z. Gu, S. Peng, J. Ma, G. Zheng, *Joule* **2018** , 2, 1610.

[25] H. Chen, Z. Yang, W. Guo, J. R. Dunlap, J. Liang, Y. Sun, K. Jie, S. Wang, J. Fu, S. Dai, *Adv. Funct. Mater.* **2019** , 29, 1906284.

[26] Q. Chang, P. Zhang, A. H. B. Mostaghimi, X. Zhao, S. R. Denny, J. H. Lee, H. Gao, Y. Zhang, H. L. Xin, S. Siahrostami, J. G. Chen, Z. Chen, *Nat. commun.* **2020** , 11, 2178.

[27] Z. Teng, Q. Zhang, H. Yang, K. Kato, W. Yang, Y.-R. Lu, S. Liu, C. Wang, A. Yamakata, C. Su, B. Liu, T. Ohno, *Nat. Catal.***2021** , 4, 374.

[28] M. Fan, J. Cui, J. Wu, R. Vajtai, D. Sun, P. M. Ajayan,*Small* **2020** , 16, 1906782.

[29] Y. J. Sa, J. H. Kim, S. H. Joo, *Angew. Chem. Int. Ed.***2019** , 58, 1100.

[30] K. Jiang, S. Back, A. J. Akey, C. Xia, Y. Hu, W. Liang, D. Schaak, E. Stavitski, J. K. Nørskov, S. Siahrostami, H. Wang, *Nat. commun.* **2019** , 10, 3997.

[321] Q. Yang, W. Xu, S. Gong, G. Zheng, Z. Tian, Y. Wen, L. Peng, L. Zhang, Z. Lu, L. Chen, *Nat. commun.* **2020** , 11, 5478.

[32] D. San Roman, D. Krishnamurthy, R. Garg, H. Hafiz, M. Lamparski, N. T. Nuhfer, V. Meunier, V. Viswanathan, T. Cohen-Karni,*ACS Catal.* **2020** , 10, 1993.

[33] S. Chen, T. Luo, K. Chen, Y. Lin, J. Fu, K. Liu, C. Cai, Q. Wang, H. Li, X. Li, J. Hu, H. Li, M. Zhu, M. Liu, *Angew. Chem. Int. Ed.* **2021** , 60, 16607.

[34] Y. Xiong, H. Li, C. Liu, L. Zheng, C. Liu, J.-O. Wang, S. Liu, Y. Han, L. Gu, J. Qian, D. Wang, *Adv. Mater.* **2022** , 34, 2110653.

[35] Z. Wang, Q.-K. Li, C. Zhang, Z. Cheng, W. Chen, E. A. McHugh, R. A. Carter, B. I. Yakobson, J. M. Tour, *ACS Catal.***2021** , 11, 2454.

[36] C. Zhang, W. Liu, M. Song, J. Zhang, F. He, J. Wang, M. Xiong, J. Zhang, D. Wang, *Appl. Catal. B Environ.* **2022** , 307, 121173.

[37] G.-F. Han, F. Li, W. Zou, M. Karamad, J.-P. Jeon, S.-W. Kim, S.-J. Kim, Y. Bu, Z. Fu, Y. Lu, S. Siahrostami, J.-B. Baek, *Nat. commun.* **2020** , 11, 2209.

[38] G. Kresse, J. Furthmüller, *Phys. Rev. B* **1996** , 54, 11169.

[39] G. Kresse, D. Joubert, *Phys. Rev. B* **1999** , 59, 1758.

[40] J. P. Perdew, J. A. Chevary, S. H. Vosko, K. A. Jackson, M. R. Pederson, D. J. Singh, C. Fiolhais, *Phys. Rev. B* **1993** , 48, 4978.

[41] R. S. Pease, *Acta Crystallogr.* **1952** , 5, 356.

[42] P. Trucano, R. Chen, *Nature* **1975** , 258, 136.

[43] J. D. Pack, H. J. Monkhorst, *Phy. Rev. B* **1977** , 16, 1748.

[44] K. Mathew, V. S. C. Kolluru, S. Mula, S. N. Steinmann, R. G. Hennig, *J. Chem. Phys.* **2019** , 151, 234101.

[45] C. Elias, P. Valvin, T. Pelini, A. Summerfield, C. J. Mellor, T. S. Cheng, L. Eaves, C. T. Foxon, P. H. Beton, S. V. Novikov, B. Gil, G. Cassabois, *Nat. Commun.* **2019** , 10, 2639.